

RESEARCH ARTICLE

10.1029/2018JD028628

Distinct Turbulence Structures in Stably Stratified Boundary Layers With Weak and Strong Surface Shear

Changxing Lan¹, Heping Liu¹, Dan Li², Gabriel G. Katul^{3,4}, and Dennis Finn⁵

Key Points:

- Stable boundary layer (SBL) states are classified by near-surface mean wind speed
- Weak and strong coupling across vertical layers form two distinct end-member states
- Distinct turbulence structures delineate these two end-member SBL states

¹Laboratory for Atmospheric Research, Department of Civil and Environmental Engineering, Washington State University, Pullman, WA, USA, ²Department of Earth and Environment, Boston University, Boston, MA, USA, ³Nicholas School of the Environment, Duke University, Durham, NC, USA, ⁴Department of Civil and Environmental Engineering, Duke University, Durham, NC, USA, ⁵NOAA Air Resources Laboratory, Idaho Falls, ID, USA

Correspondence to:

H. Liu, heping.liu@wsu.edu

Citation:

Lan, C., Liu, H., Li, D., Katul, G. G., & Finn, D. (2018). Distinct turbulence structures in stably stratified boundary layers with weak and strong surface shear. *Journal of Geophysical Research: Atmospheres*, 123. <https://doi.org/10.1029/2018JD028628>

Received 6 MAR 2018

Accepted 5 JUL 2018

Accepted article online 12 JUL 2018

Abstract Turbulence structures and exchange of momentum and heat in the nocturnal stable boundary layer (SBL) show distinct features under different stability conditions prompting interest in their connection. Here eddy covariance data collected at four different heights on a 62-m meteorological tower over a large open flat terrain are used to characterize different SBL states and associated turbulence structures. In a SBL characterized by strong near-surface winds, turbulent eddy sizes scale with their observational heights and the SBL experiences enhanced turbulent mixing of momentum and heat throughout (a state hereafter referred to as a “coupled” state). Conversely, in a decoupled SBL, weak winds occur near the surface and turbulent eddies are depressed and detached from the boundary leading to suppressed vertical mixing and layered SBL profiles. Because the transport of momentum and heat to the surface across SBL layers is determined by turbulent eddies, cross-layer correlation and the aforementioned SBL coupling states can be delineated by distinct turbulence structures.

1. Introduction

Although it is a consensus that the performance of Monin-Obukhov similarity theory (MOST) in the stable boundary layer (SBL) varies substantially with changes in stability regimes and vertical eddy structures, the mechanisms responsible for such variations remain a subject of inquiry (Mahrt, 2009, 2014; Sun et al., 2016). Unsurprisingly, efforts to examine turbulence structures and the resulting heat and momentum turbulent flux exchanges in both weakly stratified SBLs with continuous turbulence and strongly stratified SBLs with weak and intermittent turbulence have been conducted in a number of studies (Cheng & Brutsaert, 2005; Yagüe et al., 2006).

In a weakly stratified SBL with relatively strong vertical mixing, turbulence statistics can be described by MOST provided the Ozmidov length scale is much larger than z , the distance to the ground (Katul et al., 2014). In a strongly stratified SBL, however, turbulence is largely suppressed by thermal stratification in the vertical, and turbulent eddies are usually confined to thin horizontal layers resembling pancakes, leading to the so-called “ z -less” scaling (Nieuwstadt, 1984). In such regimes, the vertical flux divergence is large and leads to a non constant turbulent flux across different SBL layers (Babić, Večenaj, & DeWekker, 2016; Babić, Večenaj, Kozmar, et al., 2016). The considerable vertical flux divergence in strongly stratified SBLs results from intermittent turbulent events that can lead to nonstationary or enhanced vertical advection of momentum and scalar fluxes thereby invalidating MOST assumptions (Sun et al., 2012). The origin for these intermittent events can be partly attributed to formation of low-level jet (Karipot et al., 2008; Oldroyd et al., 2014), gravity wave (Sorbján & Czerwinska, 2013), density current (Sun et al., 2002), solitary wave (Ferreret et al., 2013), and other complicated wave-like motions (Cava et al., 2015). Elevated turbulence sources such as low-level jets result in turbulence intensity that increases with z . Hence, *upside-down* structures transport momentum and heat from elevated levels toward the ground (Acevedo et al., 2012). These frequently observed turbulent events in a strongly stratified SBL are collectively termed submeso motions (Mahrt, 2009). Such disturbance-modulated turbulence causes fluxes that deviate from predictions by MOST formulated with a suite of background state parameters (Liang et al., 2014; Sun et al., 2012).

In low wind conditions, the SBL is vertically layered with turbulence generated by local wind shear. In high wind conditions, however, the SBL is vertically connected across layers and turbulence is primarily controlled by the SBL bulk wind shear (Acevedo et al., 2016; Sun et al., 2012). Such layered and nonlayered SBLs are

sometimes referred to as decoupled and coupled states, respectively (Vickers & Mahrt, 2006), and this labeling is adopted here for consistency with nomenclature used in prior studies. Modeling studies suggest that a distinction between the coupled and the decoupled state is associated with the large-scale geostrophic wind. When the geostrophic wind is weak, the SBL is decoupled and characterized by weak or not fully developed turbulence. Cooling near the surface becomes localized and enhanced due to weak vertical mixing that then leads to further stable stratification and more turbulence suppression. However, when the geostrophic wind is strong, the SBL layers become coupled and fully turbulent, and the surface cooling is largely reduced by the enhanced turbulence transporting warm air from the upper levels to the surface (Acevedo et al., 2012; McNider et al., 1995). As a result, turbulent heat fluxes in a SBL with strong geostrophic winds are large enough to compensate the radiative cooling occurring at the surface. Those results suggest that different turbulence structures are likely responsible for the formation of coupled or decoupled states, which is the compass of the work here.

While previous studies have identified these two *coupling states* in SBLs and examined their connections with the geostrophic wind, less effort has been devoted to exploring (i) how turbulence structures (i.e., turbulent transport efficiency and turbulence scale) vary between these two distinct coupling regimes; (ii) how the SBL states affect turbulent exchange which, in turn, modulate the SBL mean profiles; and (iii) how such distinct turbulence scales influence cross-layer correlation. The main objective here is addressing these three questions using field experiments and multiscale data analysis. Data collected from four eddy covariance (EC) systems mounted on a 62-m tower are analyzed to contrast turbulence structures in SBLs with distinct coupling states. Comparison between turbulence structures across various SBL layers is experimentally examined under coupled and decoupled SBL states identified by conventional methods.

The manuscript is organized as follows: Section 2 introduces the site, instruments, and postfield data processing procedures. The results are provided in section 3, and conclusions are presented in section 4.

2. Experiment, Data, and Methodologies

2.1. Experimental Site and Instrumentation

The EC data were collected in a field campaign with 4 EC systems mounted on a 62-m tower over a flat terrain in the Idaho National Laboratory site, southeast Idaho (43.59°N, 112.94°W; 1500 m above mean sea level; Figure 1). The Idaho National Laboratory is located within a broad, relatively flat plain on the western edge of the Snake River Plain in southeast Idaho. Analyses of the historical meteorological data for the past decades showed that the boundary layer is usually dominated by southwesterly winds during the day and northeasterly winds at night (Finn et al., 2015). Under these two prevailing wind conditions, the 62-m tower has a relatively flat, uniform fetch extending many tens of kilometers upwind (Clawson et al., 2007; Finn et al., 2016). This site is covered predominantly by sagebrush and grass with a displacement height of near zero (Finn et al., 2015). The four EC systems were mounted at 2, 8, 16, and 60 m on the tower. Each EC system consisted of a 3-D sonic anemometer (CSAT3, Campbell Scientific, Inc.) to measure three-dimensional wind components and sonic derived air temperature and an infrared gas analyzer (IRGA) to measure density of water vapor and CO₂. A closed-path IRGA was mounted at 2 m (Model LI7200, LICOR Inc.), whereas three open-path IRGAs were mounted at the other three heights (Model LI7500, LICOR Inc.). Data were sampled at a frequency of 10 Hz using four dataloggers (CR5000, Campbell Scientific, Inc.) and stored for postfield processing. Additional information about this field campaign and other instrumentations are documented elsewhere (Finn et al., 2015).

2.2. Postfield Data Processing

A postfield EC data program was used to process the 10-Hz time series data from each EC system so as to obtain 30-min time-averaged statistics (Gao et al., 2016, 2017; Liu et al., 2016; Zhang & Liu, 2014). Briefly, spikes/noise were removed from the raw 10-Hz time data when Automatic Gain Control (i.e., AGC) values of the IRGAs exceeded a threshold primarily due to raindrops, dusts, and condensed water drops on the window of the IRGAs. Linear interpolation was used to replace data points with magnitude exceeding 5 times of the mean standard deviations. Sonic temperature correction was also performed using procedures described elsewhere (Liu et al., 2001; Schotanus et al., 1983). Corrections for the air density fluctuations were made for fluxes of CO₂ and latent heat, and data points were removed when they failed the quality check following the

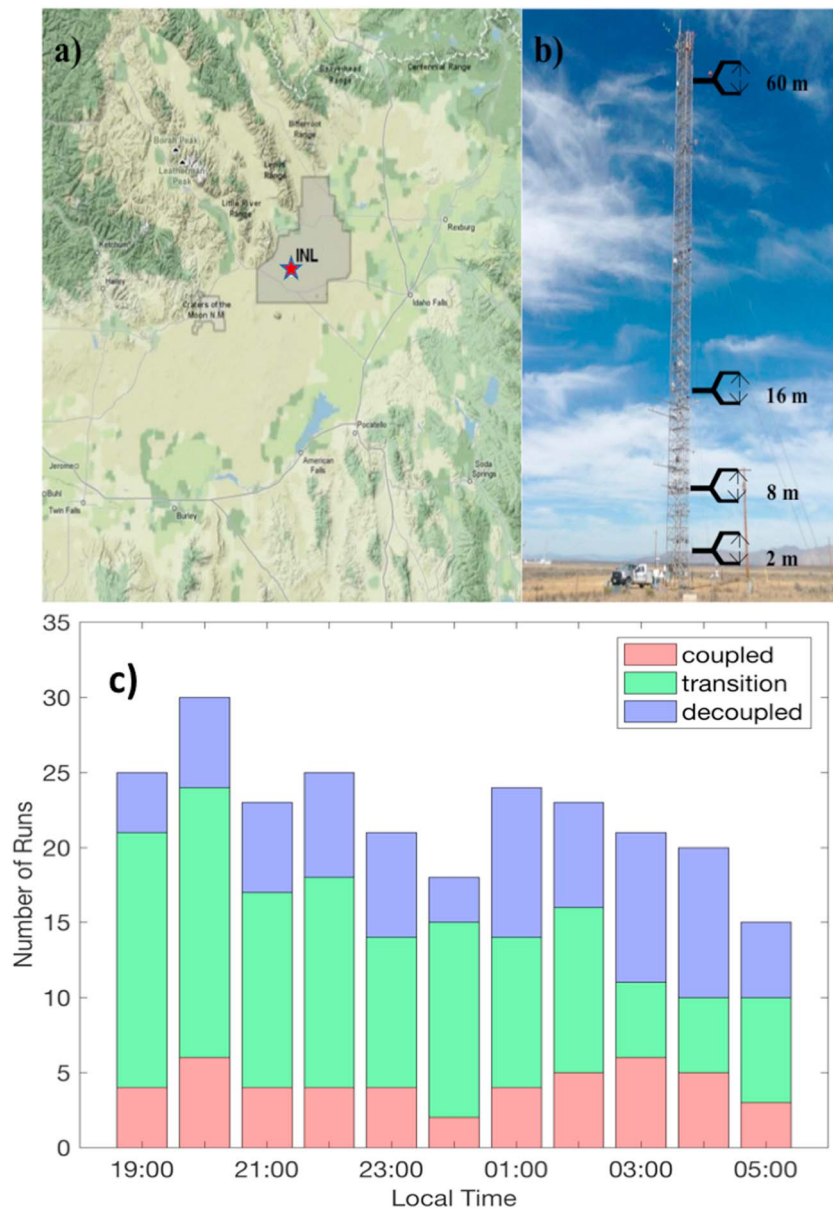


Figure 1. Project Sagebrush field site: (a) the location of the micrometeorological tower (red star) at Idaho National Laboratory (shaded; adapted from Finn et al., 2015); (b) photo showing the 64-m micrometeorological tower with the 4 EC systems; (c) number of the selected runs in each hour for the coupled (red), transition (green), and decoupled (blue) states, respectively.

method by Foken et al. (2005). Sensible heat and latent heat fluxes were obtained by calculating the mean covariance between vertical velocity fluctuations and air temperature fluctuations and between vertical velocity fluctuations and water vapor density fluctuations, respectively. Note that the 30-min statistical quantities and fluxes are computed following the procedure detailed in Sun et al. (2012). First, coordinate rotation is performed over unweighted 5-min intervals. Second, turbulent statistics and fluxes are calculated based on fluctuation quantities (i.e., u' , w' , and T') over 5-min period, then averaged to 30-min means. Therefore, these 30-min means are able to represent SBL states over a relatively long period of time and, to some extent, reduce the influence of a sudden increase or decrease in wind speeds as well as the contamination of submeso motions. One to be noted is that in strongly stable conditions, the energy and fluxes that computed by the fluctuating component may not purely contributed by turbulence even with short averaging periods (i.e., 5 min). Nonetheless, our analysis shows that the results are insensitive to

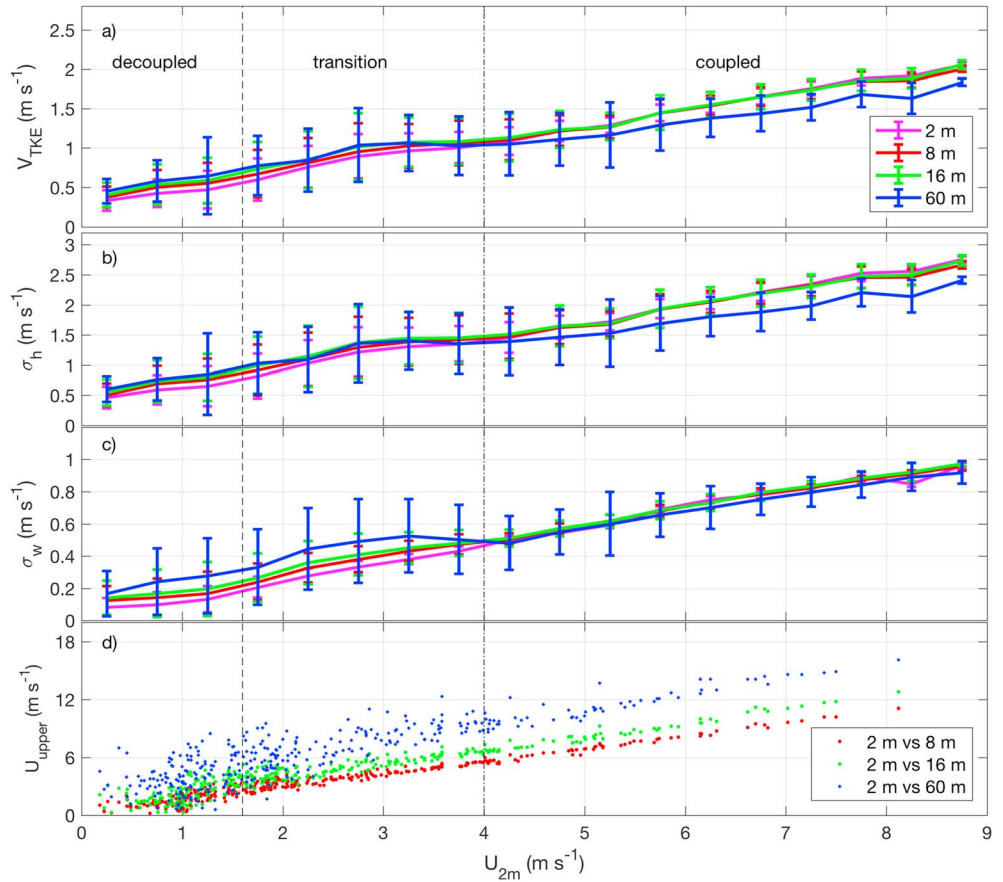


Figure 2. (a) Turbulence velocity scale (V_{TKE}) as a function of mean wind speed at 2 m; (b) horizontal component of V_{TKE} (σ_h) as a function of mean wind speed at 2 m; (c) vertical component of V_{TKE} (σ_w) as a function of mean wind speed at 2 m; (d) mean wind speeds at 8, 16, and 60 m as a function of mean wind speed at 2 m. The error bars in a, b, and c denote standard deviations. The symbols in a–c represent the bin-averaged quantities calculated by using a window width of 0.5 m/s.

the choices of averaging time (not shown). To avoid the transition period between daytime and nighttime, only nighttime data during the period from 1900 to 0600 from October 3 to November 11 in 2013 after passing quality check were used. Since extremely large values of the local nondimensional stability parameter ζ_l ($\zeta_l = z/\Lambda$, where z is the observation height and Λ is the local Obukhov length) are usually associated with sampling errors (Mahrt & Vickers, 2003), 30-min time series with ζ_l greater than 100 or smaller than zero were excluded. Based on the above data selection criteria, 245 thirty-min runs that are fairly evenly distributed over the entire nighttime period were used (Figure 1c).

3. Results and Discussion

3.1. Identification of the Coupling States Using Conventional Methods

Relations between turbulence intensity ($V_{TKE} = \sqrt{\frac{1}{2(u^2 + v^2 + w^2)}}$) and mean wind speed have been

proposed in a number of studies to categorize different turbulence regimes (Liang et al., 2014; Sun et al., 2012). To compare with these studies, a similar procedure is adopted here. The V_{TKE} at the four levels are presented as a function of the 2 m (i.e., near-surface) mean wind speed (U_{2m} ; Figure 2a). It can be seen that V_{TKE} at all four levels increase with increasing U_{2m} but the growth rate decreases with increasing z . The vertical gradient of V_{TKE} shows remarkable differences over different wind ranges. When U_{2m} is weak (i.e., $U_{2m} < 1.6$ m/s), V_{TKE} increases with height and the vertical gradient of V_{TKE} is large, suggesting that the SBL perfectly matches the classical upside-down model where the main source of

turbulence is elevated and turbulence collapses near the surface due to strong stable stratification (Mahrt, 2014). The vertical gradient of V_{TKE} between 60 m and the lower three levels decreases with an increase in U_{2m} and abruptly switches sign when U_{2m} exceeds 4 m/s. As U_{2m} further increases, V_{TKE} at 2, 8, and 16 m becomes similar, and V_{TKE} at 60 m is lower than that at the other three levels, indicating that a relatively well-mixed condition occurs between 2 and 16 m but this mixing does not reach 60 m. Therefore, the SBL with U_{2m} less than 1.6 m/s refers to the decoupled SBL, whereas the SBL with U_{2m} greater than 4 m/s refers to the coupled SBL with its coupling depth likely between 16 and 60 m. It is to be noted that these two thresholds are determined using bin-averaged quantities. At first, a window with a width of 0.5 m/s is used to calculate the bin-averaged V_{TKE} . The switch of the sign of the V_{TKE} gradient at 60 m and the similarity of V_{TKE} at the lower three levels occur when U_{2m} is 4 m/s, which is defined as the threshold separating the coupled regime and the other two regimes (Figure 2a). Then, a finer window width (0.2 m/s) is used to calculate the bin-averaged quantities in low winds ($U_{2m} < 2$ m/s). The threshold (1.6 m/s) separating the decoupled and transition states is associated with the largest V_{TKE} gradient calculated by this finer bin width. Such threshold is similar to those found in previous studies, defining a wind meandering regime with weak, intermittent turbulence (Mortarini et al., 2016; Sun et al., 2012). Since the bin-averaged fitting curves are more fluctuating when the 0.2 m/s window width is used, Figure 2 only shows the bin-averaged fitting curves with the 0.5 m/s window width. A transitional SBL is identified when U_{2m} is between 1.6 and 4 m/s. The variations of the horizontal turbulent intensity ($\sigma_h = \sqrt{\sigma_u^2 + \sigma_v^2}$) and vertical turbulent intensity (σ_w) with U_{2m} behave similarly to V_{TKE} (Figures 2b and 2c). Based on these two thresholds, 41, 125, and 79 thirty-min runs are labeled as the coupled, transition, and decoupled cases, respectively. In the decoupled state, the gradient of σ_w is larger than σ_h (i.e., the difference of σ_w between 30 and 2 m is 0.2 m/s but 0.13 m/s for σ_h). This result shows that the variations of V_{TKE} between levels mostly originate from differences in the vertical component of the turbulent intensity (σ_w) in the decoupled state. As U_{2m} increases, σ_h shows greater vertical differences than σ_w , suggesting that the differences of horizontal turbulent intensity are mainly responsible for the vertical variations of V_{TKE} in the coupled state. These results are similar to findings from the FLOSS II experiment though the aforementioned experiment did not observe a transitional SBL (Acevedo et al., 2016).

Alternatively, the decoupled and coupled SBL states are also illustrated by direct comparisons of wind speeds between the upper levels (U_{8m} , U_{16m} , and U_{60m}) and U_{2m} (Figure 2d). In a decoupled SBL, wind speeds are generally low with occasional occurrences of large winds at all the levels. Wind profiles are frequently distorted by the occurrences of possible low-level wind maxima and thus associated intermittent events, consistent with previous studies (Conangla et al., 2008; Ferreres et al., 2013). Once the SBL becomes fully coupled as a result of increased wind speeds, the intrusion of low-level wind maxima is absent and linear relations between U_{2m} and the upper levels become more evident (Figure 2d). To sum up, the delineation between coupled and decoupled SBL states at the study site appears to be reasonably captured by such conventional measures.

3.2. Turbulent Fluxes in Coupled and Decoupled SBL

The interactions between turbulent exchanges, the vertical SBL turbulent structures responsible for these exchanges, and coupling states can be illustrated by the variations of momentum and kinematic heat fluxes with the local stability parameter in coupled and decoupled states, as shown in Figure 3. It is obvious that momentum flux decreases monotonically with the increasing stability. Since it directly reflects the shear-produced turbulence, momentum flux is larger in the coupled SBL with higher wind speeds. It is greatly damped in the transitional SBL and approaches zero in the decoupled SBL with extremely weak U_{2m} (Figures 3a–3d). Some notable upward momentum fluxes at 16 and 60 m in the decoupled SBL are associated with the occurrences of low-level wind maxima below these two levels. Besides, possible contamination of submeso motions may partly account for the upward momentum fluxes (Vickers & Mahrt, 2006).

Variations of kinematic heat flux with stability show the occurrences of maximum downward heat flux under moderately stable conditions (the *turning point*). This stability turning point, which marks the transition from weakly to strongly stable regimes (Mahrt, 2016; Van De Wiel et al., 2007), increases with height. This increase of the turning point with height implies that a stronger stratification is required to offset the greater shear-generated mixing at higher levels with stronger wind speeds. Although the absolute value of kinematic

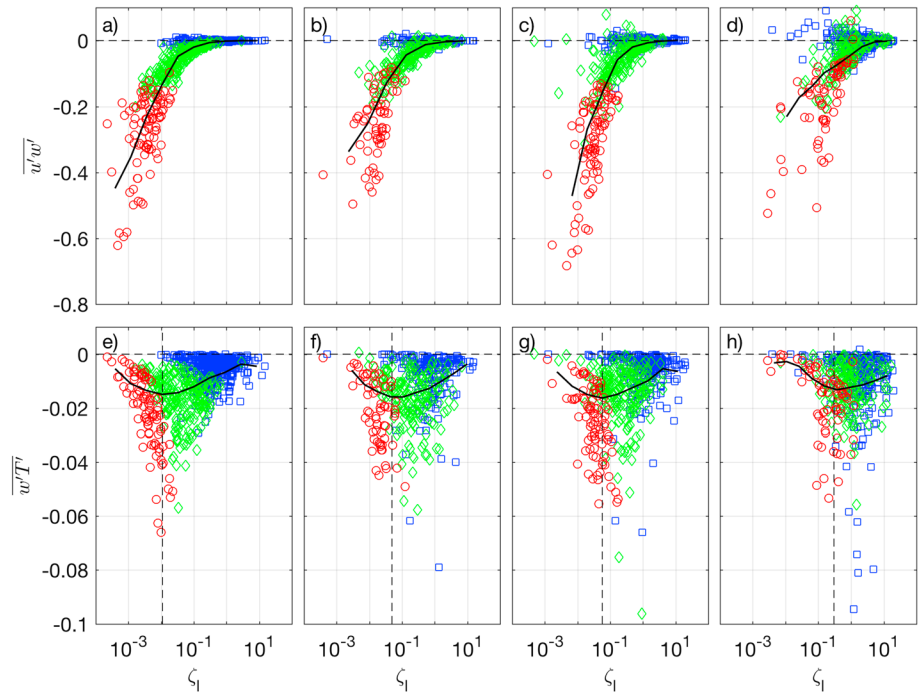


Figure 3. Variations of (top panels) momentum flux and (bottom panels) kinematic heat flux with the local atmospheric stability parameter. Panels from leftmost to rightmost correspond to results at (a and e) 2, (b and f) 8, (c and g) 16, and (d and h) 60 m. The vertical dashed lines denote the stability *turning points* for the kinematic heat fluxes, which are 0.011, 0.049, 0.057, and 0.312 for 2, 8, 16, and 60 m, respectively. The blue, green, and red symbols denote the decoupled, transitional, and coupled SBL states, respectively. The continuous black lines are the fitting curves calculated with the unweighted bin-averaged method.

heat flux decreases when the SBL becomes either much more weakly or strongly stratified (Figures 3e–3h), the underlying mechanisms are distinct. Using the flux-gradient relation, the downward heat flux ($\overline{w'T'}$) may be approximated by

$$\overline{w'T'} = -K_m Pr_t^{-1} \frac{dT}{dz} = -\left(\frac{\kappa z}{\phi_m(\zeta)}\right) u_* Pr_t^{-1} \frac{dT}{dz}, \quad (1)$$

where K_m is the momentum eddy diffusivity (i.e., given by its MOST formulation), Pr_t^{-1} is the inverse turbulent Prandtl number ($Pr_t^{-1} = K_h/K_m$, where K_h and K_m are the turbulent diffusivity for heat and momentum, respectively), dT/dz is the mean temperature gradient, κ is von Karman constant, u_* is the friction velocity, and the quantity of $\frac{\kappa z}{\phi_m(\zeta)}$ can be interpreted as reduction in the effective mixing length with increasing stability (Katul et al., 2014). Due to lack of observations of high-resolution temperature profiles, we adopt a qualitative description of Pr_t^{-1} , K_h , and K_m proposed by Katul et al. (2014) to illustrate our analysis and present the relations between $\overline{w'T'}$ and dT/dz in different SBL states (Figure 4). For weakly stable conditions, it is known that Pr_t^{-1} does not change with mild increases in the stability parameter (ζ) and the stability correction function for momentum ($\phi_m(\zeta)$) is constant and near unity (Katul et al., 2014). Under such conditions, downward heat fluxes are low due to small dT/dz despite the strong mechanically generated turbulence at high winds (Figure 4). As radiative cooling further enhances dT/dz (i.e., the averaged temperature gradient between 2 and 60 m in the transition states is 0.03 K/m), $\overline{w'T'}$ increases and reaches its maxima in the turning point primarily due to the increasing dT/dz given that adequate mechanical mixing still maintains under moderate wind speed conditions (Figure 3 versus Figure 4). After the turning point, Pr_t^{-1} dramatically decreases (at a rate faster than linear) with the increased stability due to the larger drop of K_h than K_m , which, in turn, suppresses the vertical transport of heat and favors the increase in dT/dz (i.e., the averaged temperature gradient between 2 and 60 m in the decoupled states is 0.06 K/m). In the meantime, u_* , as indicated by the momentum flux, dramatically drops as stability increases (Figures 3a–3d). As a consequence, the suppressed

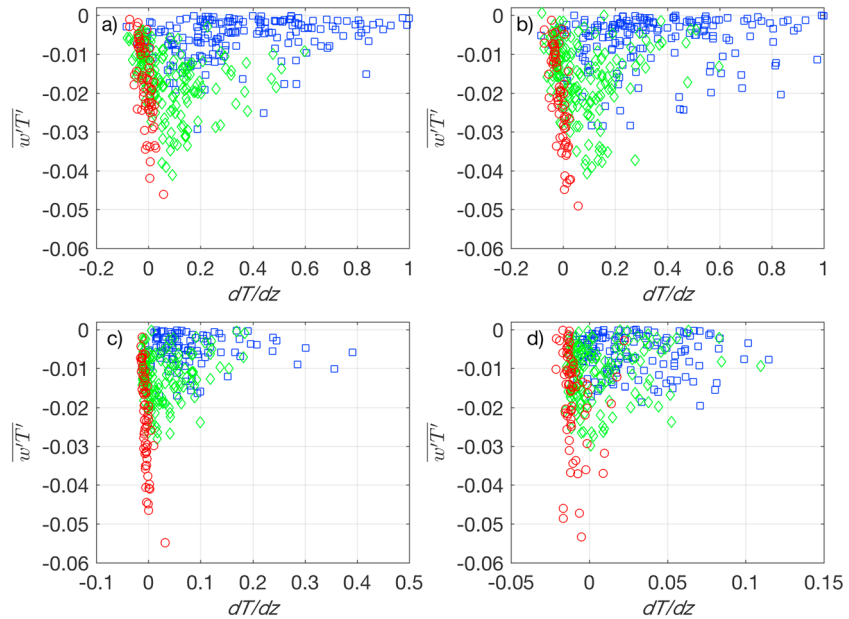


Figure 4. Variations of kinematic heat flux with the temperature gradient across two adjacent observation heights. (a–d) Results at 2, 8, 16, and 60 m, respectively. The blue, green, and red symbols denote the decoupled, transitional, and coupled SBL states, respectively.

turbulent mixing is mainly responsible for the drop of $\overline{w'T'}$ even though dT/dz is enhanced (Figure 3 versus Figure 4). The enhanced stratification further confines turbulent eddies to be within a thinner layer, leading to the decoupled SBL.

3.3. Dissimilarity Between Momentum and Heat Transport Under Different Stability Conditions

The correlation coefficient between $u'w'$ and $w'T'$ ($R_{uw, wT}$) as well as the transport efficiencies of $\overline{u'w'}$ (R_{uw}) and $\overline{w'T'}$ (R_{wT} ; defined as the correlation coefficients between u' and w' and between T' and w' , respectively) allows examination of how enhanced stability decorrelates the transport of $\overline{u'w'}$ and $\overline{w'T'}$ (Table 1). It is clear that momentum and sensible heat transport become more decorrelated in the decoupled SBL, as evidenced by the smaller value of $R_{uw, wT}$. This reflects that $\overline{u'w'}$ and $\overline{w'T'}$ are transported in a more similar way in the coupled SBL than in the decoupled SBL. This dissimilarity is also reflected by the different behaviors of $\overline{u'w'}$ and $\overline{w'T'}$ as stability increases. The magnitude of $\overline{u'w'}$ decreases dramatically

with increasing stability. However, the magnitude (absolute value) of $\overline{w'T'}$ increases with the increased stability in the coupled, weakly SBL, which is mainly attributed to the increasing temperature gradient, but decreases with the increased stability in the decoupled, strongly SBL primarily due to the greatly suppressed turbulent mixing (Figure 3). The turbulent transport efficiencies R_{uw} and R_{wT} are not appreciably different in the coupled states though $|R_{uw}| > |R_{wT}|$ across layers. This finding implies that vertical motions (w') largely regulate both momentum flux ($\overline{u'w'}$) and heat flux ($\overline{w'T'}$) in the coupled state. For the decoupled states, the data show that temperature fluctuations (T') drive vertical velocity fluctuations (w'), as reflected by $|R_{uw}| < |R_{wT}|$. One noticeable feature is that the reductions in R_{wT} are not as prominent as those in R_{uw} when the SBL changes from coupled to decoupled states. To determine the primary factors governing the variation of R_{wT} for the coupled and decoupled SBL states, the following equation is used to quantify the relative contributions from different terms:

Table 1

Averaged Correlation Coefficients Between Momentum Flux and Kinematic Heat Flux ($R_{uw, wT}$), Transport Efficiencies for the Momentum Flux (R_{uw}), and Kinematic Heat Flux (R_{wT}) in the Coupled, Transition, and Decoupled Cases

		Coupled	Transition	Decoupled
$R_{uw, wT}$	2 m	0.45	0.38	0.24
	8 m	0.43	0.36	0.23
	16 m	0.42	0.38	0.25
	60 m	0.18	0.16	0.13
R_{uw}	2 m	-0.32	-0.27	-0.13
	8 m	-0.28	-0.16	-0.08
	16 m	-0.34	-0.18	-0.06
	60 m	-0.26	-0.11	-0.08
R_{wT}	2 m	-0.16	-0.22	-0.15
	8 m	-0.19	-0.22	-0.18
	16 m	-0.21	-0.23	-0.15
	60 m	-0.16	-0.19	-0.16

$$-\frac{d|R_{wT}|}{|R_{wT}|} = -\frac{d|\overline{w'T'}|}{|\overline{w'T'}|} + \frac{d\sigma_T}{\sigma_T} + \frac{d\sigma_w}{\sigma_w}, \quad (2)$$

where $-\frac{d|R_{wT}|}{|R_{wT}|}$ refers to the variation of the transport efficiency and $-\frac{d|\overline{w'T'}|}{|\overline{w'T'}|}$, $\frac{d\sigma_T}{\sigma_T}$, and $\frac{d\sigma_w}{\sigma_w}$ represent the relative

changes in kinematic heat flux, standard deviation for temperature, and standard deviation for vertical velocity, respectively. Calculations confirm that the nearly constant R_{wT} from coupled to decoupled states is largely attributed to the enhanced σ_T due to the increased dT/dz that actively regulates vertical velocity

fluctuations. For example, at 2 m, $\frac{d\sigma_T}{\sigma_T} = 1.75$, but $-\frac{d|\overline{w'T'}|}{|\overline{w'T'}|} = 0.67$ and $\frac{d\sigma_w}{\sigma_w} = 0.84$.

To elaborate further on this point, consider the stationary temperature variance budget for a planar homogeneous flow in the absence of subsidence (imposed by coordinate rotation here). This budget is given by

$$\frac{\partial \sigma_T^2}{\partial t} = 0 = -2\overline{w'T'} \frac{\partial T}{\partial z} - \frac{\partial \overline{w'w'T'}}{\partial z} - 2\epsilon_{TT} \quad (3)$$

If the temperature variance dissipation rate scales as $\epsilon_{TT} = \frac{C_{TT}\sigma_T^2}{\tau}$, where τ is a relaxation time scale given by the TKE and its dissipation rate and the flux transport term is momentarily ignored, then

$$\sigma_T^2 = \frac{\tau}{C_{TT}} \overline{w'T'} \frac{\partial T}{\partial z} \quad (4)$$

This analysis shows that dT/dz partly dictates σ_T^2 and the decline in $\overline{w'T'}$ and τ equally contributes to the σ_T^2 variations. This may be one reason why $\frac{d\sigma_T}{\sigma_T}$ exceeds $-\frac{d|\overline{w'T'}|}{|\overline{w'T'}|}$ and $\frac{d\sigma_w}{\sigma_w}$. The large reduction in R_{uw} is mainly due to the suppression of vertical turbulent fluctuation induced by the enhanced dT/dz .

3.4. Turbulent Transport Efficiencies and Structures Across Layers in Two SBL Coupling States

It is expected that turbulent transfer with comparable transport efficiencies of momentum and scalars at different levels indicate a relatively well-mixed condition across layers and thus a coupled SBL. Therefore, comparisons of transport efficiencies of momentum and scalars across layers can illustrate the role of turbulence structures in regulating different SBL coupling states with stability. As indicated by the comparisons of R_{uw} (Figures 5a–5c) and R_{wT} (Figures 5d–5f) between the three upper levels and 2 m, a convergence of data points to the 1:1 line suggests comparable transport efficiencies throughout the coupled SBL, whereas the large scatter in the decoupled SBL indicates that fluxes are transported by different turbulent eddies with distinct efficiencies across layers. In the decoupled SBL, turbulent transport of momentum and heat at different levels can have opposite directions as evidenced by the data points scattered across the different quadrants. The opposite transport directions may be partly caused by the erratic fluxes induced by submeso motions.

To further illustrate the differences in turbulence structures between the coupled and decoupled SBLs, fast Fourier transform is employed to determine the average u , v , and w power spectra as well as the average uw and wT cospectra as a function of nondimensional frequency ($n = fz/U$, where f is natural frequency, z is height, and U is mean wind speed; Figure 6). Note that for each data run, coordinate rotation and calculation of fluctuation quantities are performed over the 30-min period. For the coupled cases, the normalized u and v spectra at 2, 8, and 16 m show a similar peak energy that are greater than those at 60 m. This finding is consistent with the above results that turbulence intensities at 2, 8, and 16 m are similar but greater than at 60 m in such regimes. The difference in the frequencies associated with the peak u and v spectra energy across levels is attributed to the different horizontal scales of turbulent

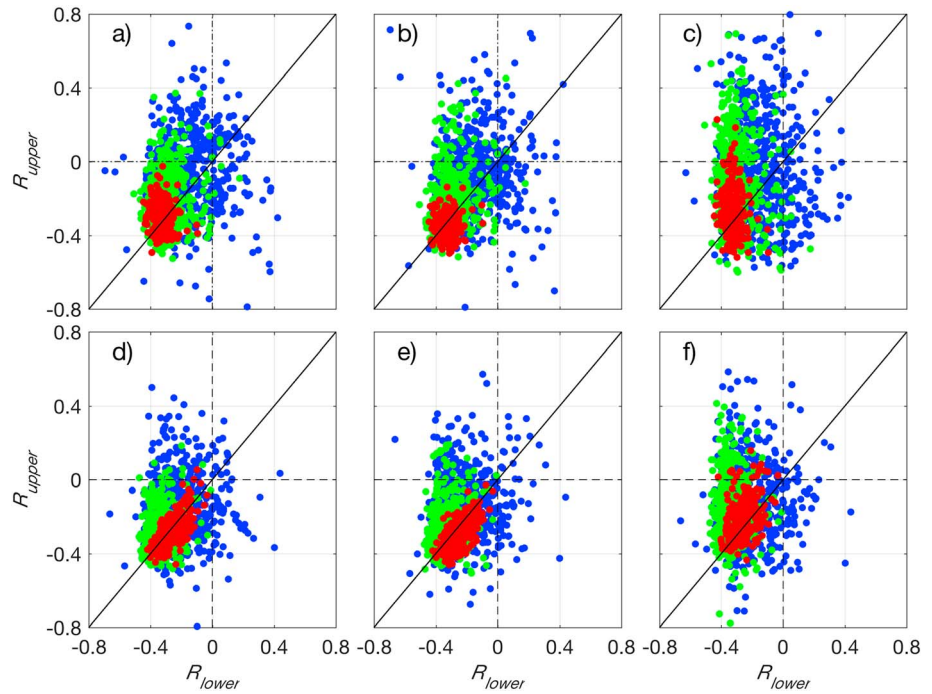


Figure 5. Comparisons of turbulence transport efficiency for (top panels) momentum and (bottom panels) kinematic heat fluxes between the three upper levels and 2 m (left panels: 8 m; middle panels: 16 m; right panels: 60 m). The blue, green, and red symbols represent decoupled, transition, and coupled SBL states, respectively.

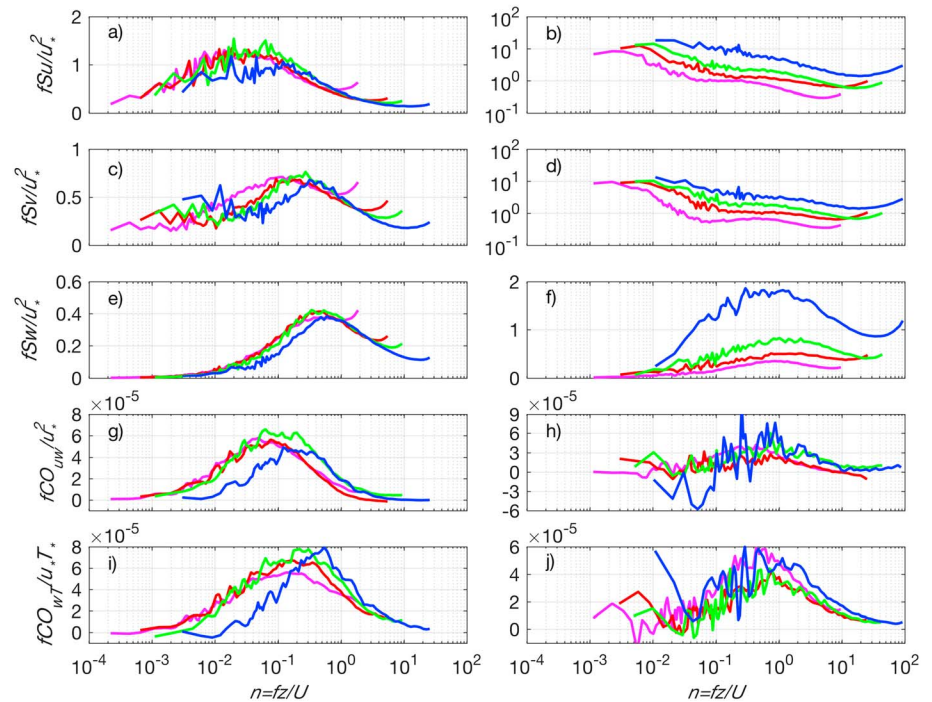


Figure 6. Normalized averaged spectra and cospectra of (a and b) u , (c and d) v , (e and f) w , (g and h) $u-w$, and (i and j) $w-T$. The left and right panels represent the coupled and decoupled SBL states, respectively. The magenta, red, green, and blue lines represent spectra or cospectra for 2, 8, 16, and 60 m, respectively. Spectrum and cospectrum for each 30-min run are normalized by the 2 m scaling parameters before averaging.

Table 2

Nondimensional Frequency ($n = fz/\bar{U}$) and Length Scales ($L = \bar{U}/f$, f is the Natural Frequency) Associated With Peak Velocity Spectra Energy in the Coupled and Decoupled Cases

		u		v		w	
		n	L (m)	n	L (m)	n	L (m)
2 m	Decoupled	0.11	18.2	0.50	4.0	0.97	2.1
	Coupled	0.01	140.5	0.12	16.3	0.42	4.8
8 m	Decoupled	0.10	76.8	0.86	9.3	1.69	4.7
	Coupled	0.04	190.5	0.16	48.5	0.44	18.1
16 m	Decoupled	0.10	154.8	0.41	39.4	1.17	13.7
	Coupled	0.07	224.0	0.23	71.1	0.43	37.0
60 m	Decoupled	0.20	304.6	0.94	64.1	1.30	46.0
	Coupled	0.12	487.5	0.40	166.7	0.67	89.2

eddies. Despite the small difference in w spectra at 60 m as a result of the shallow coupling depth, the peak spectra energy for w are not only comparable but also occur at almost the same frequency, suggesting the possible influence of the same active turbulent eddies across layers. In addition, the less-than-one frequencies for the spectra peaks indicate that the vertical scales of turbulent eddies are larger than their observational heights (Sun et al., 2012). Therefore, those active turbulent eddies do interact with the surface directly, transporting momentum and heat with similar efficiencies across layers, and thus resulting in a coupled SBL. Note that the vertical velocity spectra across the different heights overlap in the inertial subrange suggesting that the surface scaling parameters can describe turbulence in the coupled SBL. Except for 60 m, the uw and wT cospectra at 2, 8, and 16 m exhibit similar patterns with the same peak values in the same frequency intervals.

For the decoupled cases, the u , v , and w spectral magnitudes increase with heights, consistent with the observed features that turbulence intensity is enhanced with increasing heights. For the u and v spectra, the increasing spectra energy at low-frequency ranges indicates the influence of quasi-horizontal submeso motions (i.e., meandering) that greatly impact the horizontal flow field. The frequencies for the peak w spectra are greater than 1 implying that turbulent eddies are detached from the surface. These distinct characteristics of turbulent eddies across layers result in the absence of well-defined cospectral peaks with a similar frequency. Moreover, the contamination of submeso motions is also evidenced by the oscillating signs at low-frequency ranges of the cospectra (Cava et al., 2016; Mahrt, 2009).

As summarized in Table 2 about the frequencies (n) and length scales ($L = \bar{U}/f$, f is the natural frequency) associated with the peak spectra energy, turbulent eddies have larger sizes in the coupled SBL and have larger horizontal scales with heights as compared with the decoupled SBL. Only in the coupled SBL are the vertical scales of turbulent eddies comparable to their observational heights. In the decoupled SBL, the vertical scales of turbulent eddies measured at 8, 16, and 60 m are not only smaller than the observational heights but also smaller than the distances between any two adjacent levels (i.e., turbulence appears to be governed by fine-scale eddies).

3.5. Cross-Layer Correlation in Two SBL Coupling States

Higher cross-layer correlations are expected to occur in the coupled SBLs as different vertical layers are experiencing the same active turbulent eddies with vertical scales comparable to z . In the decoupled SBLs, however, the cross-layer correlation is likely to be poor since turbulent eddies are vertically suppressed and only generate weak mixing in a locally thin layer. To provide a visual comparison, two time series with one in the coupled state and the other in the decoupled state are directly compared (Figure 7). For the coupled case (0230–0300 MST on 14 October; the left panels in Figure 7), the simultaneous occurrences of peaks and valleys are evident at different levels not only in the wind and temperature fields (u' , T' , and w') but also in the time series of instantaneous fluxes ($u'w'$ and $w'T'$). For the decoupled cases (0300–0330 MST on 22 October; the right panels in Figure 7), however, distinct fluctuating patterns occur at different heights suggesting layered vertical structures in the strongly SBL.

To further illustrate turbulence structures in a manner that simultaneously identifies the temporal scale and occurrence time location, the continuous wavelet transform is employed (Gao et al., 2016) to analyze the time series of turbulence fluctuations (i.e., u' , w' , and T') for the coupled and decoupled cases presented in Figure 7. For an arbitrary series $f(t)$, the wavelet coefficient can be determined by

$$W(\lambda, t) = \int_{-\infty}^{+\infty} f(x) * \psi_{\lambda, t}(x) dx, \quad (5)$$

where $\psi_{\lambda, t}(x)$ is the mother wavelet expressed as $\psi_{\lambda, t}(x) = \frac{1}{\sqrt{\lambda}} * \psi(\frac{x-t}{\lambda})$; t and λ are the location and scale parameters, respectively; and $W(\lambda, t)$ is the wavelet coefficient as a function of time and scales. The Morlet wavelet, which is symmetric and reasonably localized in the time and frequency domains, is used to process the detrended and normalized 10-Hz time series for the 30-min runs. The temporal (x axis) and scale (y axis) distribution of the wavelet coefficient (i.e., $W(\lambda, t)$ in equation (5)) relative to u' and w' is shown in Figures 8 and 9,

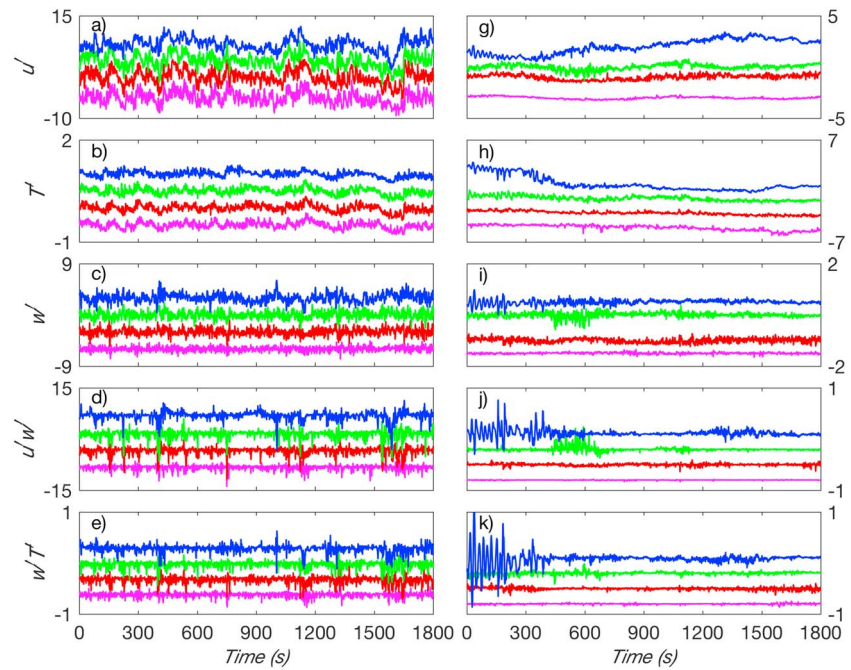


Figure 7. The 30-min, 10-Hz time series of (a and g) u' , (b and h) T' , (c and i) w' , (d and j) $u'w'$, and (e and k) $w'T'$ for the coupling case (left panels) and decoupling case (right panels). The magenta, red, green, and blue lines represent 2, 8, 16, and 60 m, respectively. Fluctuations at 8, 16, and 60 m are shifted upward for readability.

respectively. Positive (and negative) wavelet coefficients are associated with positive (and negative) fluctuations, respectively, in the time series shown in Figure 7. We focus on those organized structures with time scales ranging from 50 to 300 s rather than the disorganized structures with time scales of less

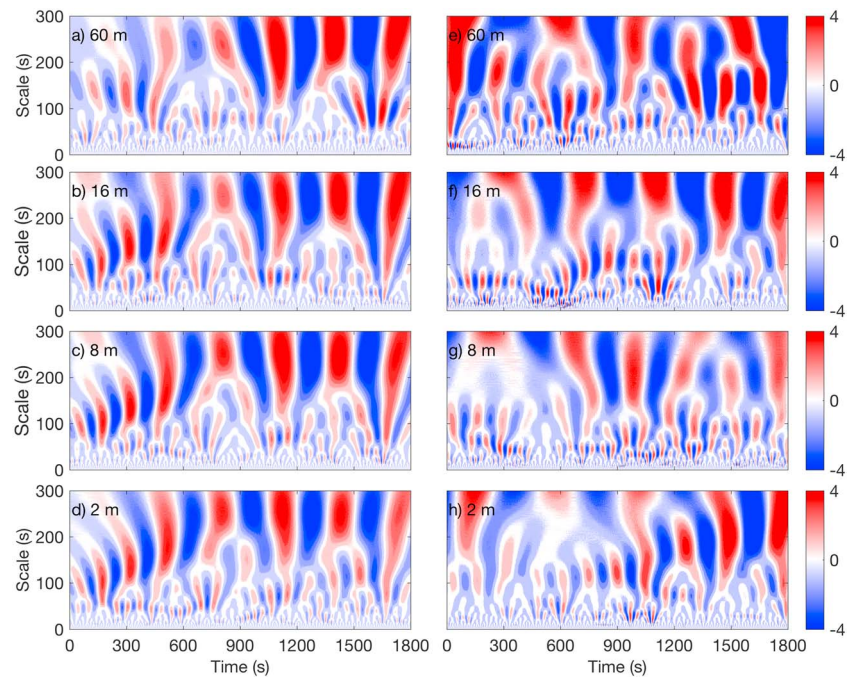


Figure 8. The time and scale distributions of the wavelet coefficients (i.e., W in equation (5)) for the 30-min, 10-Hz time series of u' . Left panels and right panels represent the coupling and decoupling cases, respectively, for (a and e) 60, (b and f) 16, (c and g) 8, and (d and h) 2 m.

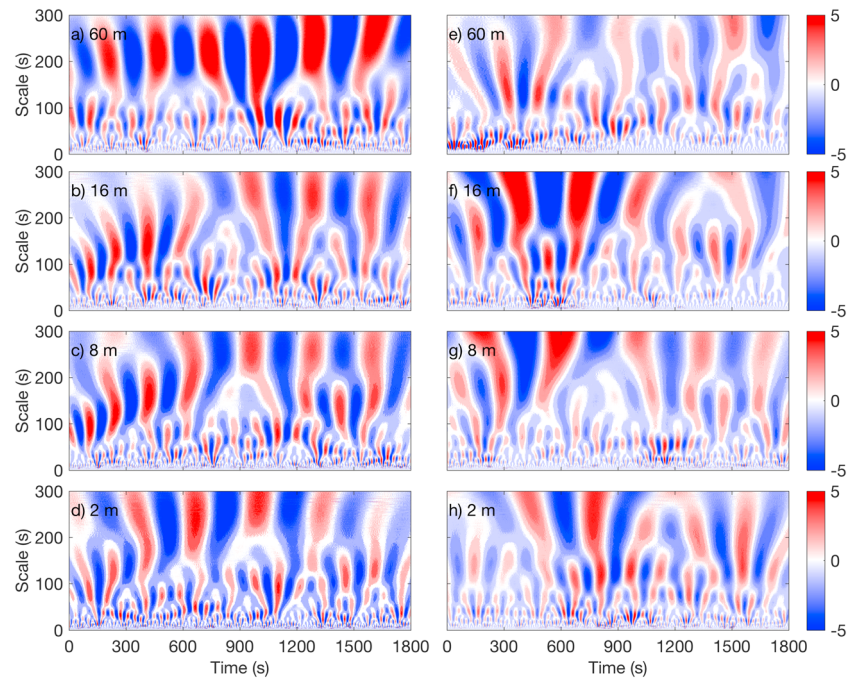


Figure 9. The time and scale distributions of the wavelet coefficients (i.e., W in equation (5)) for the 30-min, 10-Hz time series of w' . Left panels and right panels represent the coupling and decoupling cases, respectively, for (a and e) 60, (b and f) 16, (c, g) 8, and (d and h) 2 m.

than 50 s. As the time scale increases, well-organized plume-like patterns are shown in Figure 8a (i.e., plume-like shapes at about 400 s in Figure 8a). Large positive (red color) and negative (blue color) centers, respectively, represent active eddies contributing to the peaks and valleys in the time series shown in Figure 7. In the coupled case, the positive and negative centers at different heights not only occur almost at the same time but also have similar time scales, whereas in the decoupled case the positive and negative centers with similar time scales rarely occur simultaneously across layers. Note that a number of organized structures appear at both 16 and 8 m simultaneously in the decoupled case (i.e., Figures 8f and 8g, between 600–900 s with the time scale of 100–300 s), but they fail to reach $z = 2$ m due to the strong stratification in near-surface layer. These observed features further confirm previous findings (here and in the literature) that in the coupled SBL, the whole SBL is dominated by the same active turbulent eddies that interact with the surface, whereas turbulent eddies in the decoupled SBL are localized, detached from the surface, and only occasionally affect some adjacent layers.

As a proxy of cross-layer correlation, the simultaneous occurrences of such active turbulent eddies across vertical layers is further quantified by calculating the average correlation coefficients of the 30-min wavelet coefficients with the time scales of 200 to 300 s for u' , w' , and T' between the 60 m and other three lower levels in the coupled and decoupled SBL states. Clearly, the correlation coefficients of wavelet coefficients for u' , w' , and T' in the coupled cases are greater than those in the decoupled cases, indicating that the coupled states show better cross-layer correlation since turbulent eddies have larger vertical scales and generate stronger vertical mixing throughout the SBL (Figure 10). To further investigate the dominant scales of turbulent eddies that modulate cross-layer correlation, we examine the correlation coefficients across different scales (i.e., 50–100 s, 100–200 s, and 200–300 s). In general, for different scale ranges, the comparisons of $R_{u'}$, $R_{w'}$, and $R_{T'}$ between the coupled and decoupled cases are similar as those shown in Figure 10. One interesting feature is found in the correlation coefficients of w' . $R_{w'}$ at time scales ranging from 200 to 300 s shows a large difference between coupled and decoupled cases; while at smaller scales, $R_{w'}$ is comparable between coupled and decoupled cases (not shown). It suggests that turbulent motions with scales ranging from 200 to 300 s are primarily responsible for the cross-layer correlation. It is also the reason why Figure 10 only presents the correlation coefficients with time scales of 200–300 s.

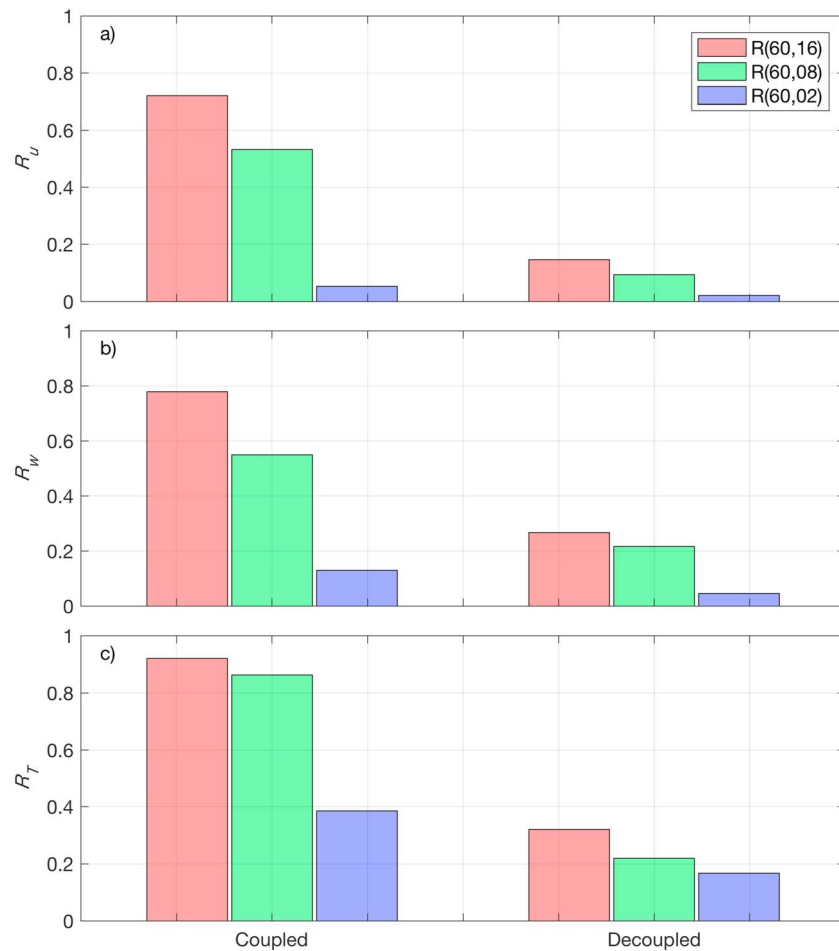


Figure 10. Averaged correlation coefficients of wavelet coefficients with time scales of 200–300 s for 30-min, 10-Hz time series of u' , w' , and T' between the 60 m and the three lower levels for the coupling and decoupling cases. (a–c) The correlation coefficients of wavelet transform coefficients with time scales ranging from 200 to 300 s. The red, green, and blue bars in each panel represent the correlation coefficients of wavelet coefficient series between 60 and 16 m, 60 and 8 m, and 60 and 2 m, respectively.

3.6. A Schematic Overview

The relations between these two distinct end-member SBL states and the associated turbulence structures can be summarized by a schematic diagram in Figure 11. In the decoupled SBL with weak surface shear (Figure 11a), turbulence is primarily generated near the level where the low-level jet nose is located (analogous to an inverted boundary layer). Turbulent eddies with moderate scales, which occur in elevated levels below the jet nose, have limited influence on turbulence generation in the lower levels (analogous to mechanical production of TKE scaling inversely with the distance below the jet nose). As a result, turbulent eddies are confined within a thin layer, leading to the suppressed downward transport of momentum and heat. In turn, such weak vertical mixing favors a buildup of more strongly stratified SBL due to radiative cooling. It is in agreement with a previous study that investigated a complex nighttime case of how the development of LLJ triggered wave-like submeso motions and strongly influenced turbulent mixing, resulting in a layered SBL (Mortarini et al., 2018). Another variant on the decoupled end-member state is associated with the occurrence of wind direction shear (Figure 11b). Although the LLJ is absent, the aloft wind direction shear also enhances turbulence. These enhanced turbulent eddies are usually unable to penetrate further downward, resulting in a suppressed downward momentum and heat transport, and thus an even more decoupled, layered SBL. In the coupled SBL with strong surface shear (Figure 11c), the strong mechanical shear (produced near the ground) favors the development of turbulent eddies with larger scales that enhance vertical mixing of momentum and heat. Such stronger mixing can effectively prevent the buildup

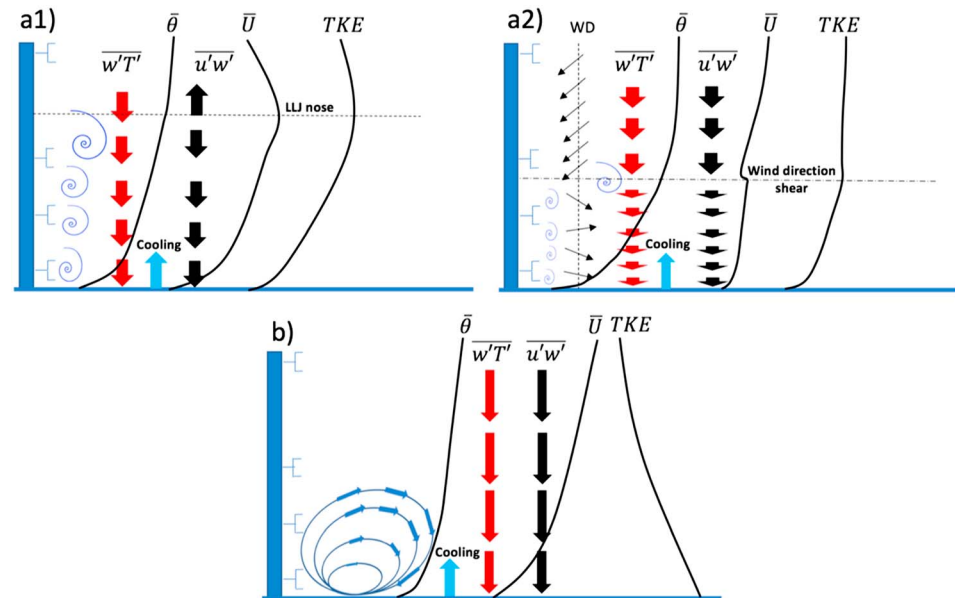


Figure 11. Schematic illustration showing two end-member states of SBL and the characteristic sizes of turbulent eddies in these two distinct SBL coupling states. (a1) Decoupled, strongly SBL with intrusion of low-level jet (LLJ), which represents a structure resembling an *upside-down* boundary layer. The horizontal dash line denotes the height of the LLJ nose. (a2) Extremely decoupled, strongly SBL with large wind direction shear occurring within a layer of tens of meters. A shallow near surface with wind direction shear is beneath a deep, prevailing flow. The horizontal dash-dot line denotes the height with the largest wind direction shear and turbulence production. In this situation, turbulence generated by wind direction shear is very weak and turbulent fluxes are small, leading to a complete decoupled SBL. (b) Coupled, weakly SBL characterized by conventional lognormal mean wind profile. The black and red arrows represent direction and magnitude of momentum flux and sensible heat flux transport. The blue arrows with different sizes represent different extent of radiative cooling effect in two SBL states.

of stable stratification induced by surface radiative cooling through effectively transporting the warm air aloft downward and the surface cold air upward. As a result, the weakened stratification allows turbulent eddies to further develop, maintaining a well coupled SBL across layers.

4. Conclusions

Two distinct SBL states and associated turbulence structures were observed and analyzed above a flat and uniform ground surface. In the decoupled SBL state, turbulence is primarily generated aloft and collapses near the surface. Momentum and heat fluxes exhibit different behavior as stability increases. With strong surface shear, the mechanical mixing weakens the magnitude of mean temperature gradient and allows turbulent eddies with larger vertical scales to develop. The magnitude of downward sensible heat flux is mainly dependent on the small vertical temperature gradient and the large turbulent heat diffusivity. In such scenario, turbulent eddies result in high cross-layer correlations among turbulent flow variables responsible for heat and momentum transport. On the contrary, under weak surface shear conditions, the weak mechanical mixing favors the buildup of strong stratifications, induced by the surface radiative cooling, which in turn confines turbulent eddies within thin layers locally. Such suppressed turbulent eddies are responsible for the limited downward heat flux, weakened vertical mixing, poor cross-layer correlation, and thus the formation of decoupled SBL state with enhanced stable stratifications.

References

- Acevedo, O. C., Costa, F. D., & Degrazia, G. A. (2012). The coupling state of an idealized stable boundary layer. *Boundary-Layer Meteorology*, 145(1), 211–228. <https://doi.org/10.1007/s10546-011-9676-3>
- Acevedo, O. C., Mahrt, L., Puhales, F. S., Costa, F. D., Medeiros, L. E., & Degrazia, G. A. (2016). Contrasting structures between the decoupled and coupled states of the stable boundary layer. *Quarterly Journal of the Royal Meteorological Society*, 142(695), 693–702. <https://doi.org/10.1002/qj.2693>
- Babić, N., Večenaj, Ž., & DeWekker, S. F. J. (2016). Flux–variance similarity in complex terrain and its sensitivity to different methods of treating non-stationarity. *Boundary-Layer Meteorology*, 159(1), 123–145. <https://doi.org/10.1007/s10546-015-0110-0>

Acknowledgments

We wish to acknowledge S. Beard, T. Strong, and B. Reese from the Field Research Division of NOAA as well as E. Russell and Z. Gao for their assistance during the field campaign. We thank Dr. Daniela Cava and two anonymous reviewers for their constructive comments to improve the quality of this manuscript. H. Liu acknowledges support by National Science Foundation (NSF-AGS-1419614). C. Lan acknowledges support by China Scholarship Council (CSC) and National Science Foundation (NSF-AGS-1419614). G. Katul also acknowledges support from NSF (NSF-EAR-1344703, NSF-AGS-1644382, and NSF-DGE-1068871) and from the Department of Energy (DE-SC-0011461). According to the AGU publications Data Policy, the data used in this paper are deposited in a public repository (http://micromet.paccar.wsu.edu/paperdata/FluxData_30min.xlsx).

- Babić, N., Večenaj, Ž., Kozmar, H., Horvath, K., De Wekker, S. F. J., & Grisogono, B. (2016). On turbulent fluxes during strong winter bora wind events. *Boundary-Layer Meteorology*, *158*(2), 331–350. <https://doi.org/10.1007/s10546-015-0088-7>
- Cava, D., Giostra, U., & Katul, G. (2015). Characteristics of gravity waves over an antarctic ice sheet during an Austral summer. *Atmosphere*, *6*(9), 1271–1289. <https://doi.org/10.3390/atmos6091271>
- Cava, D., Mortarini, L., Giostra, U., Richiardone, R., & Anfossi, D. (2016). A wavelet analysis of low-wind-speed submeso motions in a nocturnal boundary layer. *Quarterly Journal of the Royal Meteorological Society*, *143*(703), 661–669. <https://doi.org/10.1002/qj.2954>
- Cheng, Y., & Brutsaert, W. (2005). Flux-profile relationships for wind speed and temperature in the stable atmospheric boundary layer. *Boundary-Layer Meteorology*, *114*(3), 519–538. <https://doi.org/10.1007/s10546-004-1425-4>
- Clawson, K. L., Eckman, R. M., Hukari, N. F., Rich, J. D., & Ricks, N. R. (2007). Climatology of the Idaho National Laboratory 3RD Edition NOAA Technical Memorandum OAR ARL-259, Air Resources Laboratory, Idaho Falls, Idaho. (240 pp).
- Conangla, L., Cuxart, J., & Soler, M. R. (2008). Characterisation of the nocturnal boundary layer at a site in northern Spain. *Boundary-Layer Meteorology*, *128*(2), 255–276. <https://doi.org/10.1007/s10546-008-9280-3>
- Ferreres, E., Soler, M. R., & Terradellas, E. (2013). Analysis of turbulent exchange and coherent structures in the stable atmospheric boundary layer based on tower observations. *Dynamics of Atmospheres and Oceans*, *64*, 62–78. <https://doi.org/10.1016/j.dynatmoce.2013.10.002>
- Finn, D., Clawson, K. L., Eckman, R. M., Carter, R. G., Rich, J. D., Strong, T. W., et al. (2015). Project Sagebrush Phase 1, NOAA Technical Memorandum OAR ARL-268, Air Resources Laboratory, Idaho Falls, Idaho (338 pp.). <https://doi.org/10.7289/V5VX0DHV>
- Finn, D., Reese, B., Butler, B., Wagenbrenner, N., Clawson, K. L., Rich, J., et al. (2016). Evidence for gap flows in the Birch Creek Valley, Idaho. *Journal of the Atmospheric Sciences*, *73*(12), 4873–4894. <https://doi.org/10.1175/JAS-D-16-0052.1>
- Foken, T., Gööckede, M., Mauder, M., Mahrt, L., Amiro, B., & Munger, W. (2005). Post-field data quality control. In X. Lee, W. Massman, & B. Law (Eds.), *Handbook of Micrometeorology: A Guide for Surface Flux Measurement and Analysis* (pp. 181–208). Dordrecht, Netherlands: Springer. https://doi.org/10.1007/1-4020-2265-4_9
- Gao, Z., Liu, H., Katul, G. G., & Foken, T. (2017). Non-closure of the surface energy balance explained by phase difference between vertical velocity and scalars of large atmospheric eddies. *Environmental Research Letters*, *12*(3), 34025. <https://doi.org/10.1088/1748-9326/aa625b>
- Gao, Z., Liu, H., Russell, E. S., Huang, J., Foken, T., & Oncley, S. P. (2016). Large eddies modulating flux convergence and divergence in a disturbed unstable atmospheric surface layer. *Journal of Geophysical Research: Atmospheres*, *121*, 1475–1492. <https://doi.org/10.1002/2015JD024529>
- Karipoti, A., Leclerc, M. L., Zhang, G., Lewin, K. F., Nagy, J., Hendrey, G. R., & Starr, G. (2008). Influence of nocturnal low-level jet on turbulence structure and CO₂ flux measurements over a forest canopy. *Journal of Geophysical Research*, *113*, D10102. <https://doi.org/10.1029/2007JD009149>
- Katul, G. G., Porporato, A., Shah, S., & Bou-Zeid, E. (2014). Two phenomenological constants explain similarity laws in stably stratified turbulence. *Physical Review E*, *89*(2), 023007. <https://doi.org/10.1103/PhysRevE.89.023007>
- Liang, J., Zhang, L., Wang, Y., Cao, X., Zhang, Q., Wang, H., & Zhang, B. (2014). Turbulence regimes and the validity of similarity theory in the stable boundary layer over complex terrain of the Loess Plateau, China. *Journal of Geophysical Research: Atmospheres*, *119*, 6009–6021. <https://doi.org/10.1002/2014JD021510>
- Liu, H., Peters, G., & Foken, T. (2001). New equations for sonic temperature variance and buoyancy heat flux with an omnidirectional sonic anemometer. *Boundary-Layer Meteorology*, *100*(3), 459–468. <https://doi.org/10.1023/A:1019207031397>
- Liu, H., Zhang, Q., Katul, G. G., Cole, J. J., Chapin, F. S. III, & MacIntyre, S. (2016). Large CO₂ effluxes at night and during synoptic weather events significantly contribute to CO₂ emissions from a reservoir. *Environmental Research Letters*, *11*(6), 64001. <https://doi.org/10.1088/1748-9326/11/6/064001>
- Mahrt, L. (2009). Characteristics of submeso winds in the stable boundary layer. *Boundary-Layer Meteorology*, *130*(1), 1–14. <https://doi.org/10.1007/s10546-008-9336-4>
- Mahrt, L. (2014). Stably stratified atmospheric boundary layers. *Annual Review of Fluid Mechanics*, *46*(1), 23–45. <https://doi.org/10.1146/annurev-fluid-010313-141354>
- Mahrt, L. (2016). Heat flux in the strong-wind nocturnal boundary layer. *Boundary-Layer Meteorology*, *163*(2), 161–177. <https://doi.org/10.1007/s10546-016-0219-9>
- Mahrt, L., & Vickers, D. (2003). Formulation of turbulent fluxes in the stable boundary layer. *Journal of the Atmospheric Sciences*, *60*(20), 2538–2548. [https://doi.org/10.1175/1520-0469\(2003\)060<2538:FOTFIT>2.0.CO;2](https://doi.org/10.1175/1520-0469(2003)060<2538:FOTFIT>2.0.CO;2)
- McNider, R. T., England, D. E., Friedman, M. J., & Shi, X. (1995). Predictability of the stable atmospheric boundary layer. *Journal of the Atmospheric Sciences*, *52*(10), 1602–1614. [https://doi.org/10.1175/1520-0469\(1995\)052<1602:POTSAB>2.0.CO;2](https://doi.org/10.1175/1520-0469(1995)052<1602:POTSAB>2.0.CO;2)
- Mortarini, L., Cava, D., Giostra, U., Acevedo, O., Nogueira Martins, L. G., Soares de Oliveira, P. E., & Anfossi, D. (2018). Observations of submeso motions and intermittent turbulent mixing across a low level jet with a 132-m tower. *Quarterly Journal of the Royal Meteorological Society*, *144*(710), 172–183. <https://doi.org/10.1002/qj.3192>
- Mortarini, L., Stefanello, M., Degrazia, G., Roberti, D., Trini Castelli, S., & Anfossi, D. (2016). Characterization of wind meandering in low-wind-speed conditions. *Boundary-Layer Meteorology*, *161*(1), 165–182. <https://doi.org/10.1007/s10546-016-0165-6>
- Nieuwstadt, F. T. M. (1984). The turbulent structure of the stable, nocturnal boundary layer. *Journal of the Atmospheric Sciences*, *41*(14), 2202–2216. [https://doi.org/10.1175/1520-0469\(1984\)041<2202:TTSOTS>2.0.CO;2](https://doi.org/10.1175/1520-0469(1984)041<2202:TTSOTS>2.0.CO;2)
- Oldroyd, H. J., Katul, G., Pardyjak, E. R., & Parlange, M. B. (2014). Momentum balance of katabatic flow on steep slopes covered with short vegetation. *Geophysical Research Letters*, *41*, 4761–4768. <https://doi.org/10.1002/2014GL060313>
- Schotanus, P., Nieuwstadt, F. T. M., & De Bruin, H. A. R. (1983). Temperature measurement with a sonic anemometer and its application to heat and moisture fluxes. *Boundary-Layer Meteorology*, *26*(1), 81–93. <https://doi.org/10.1007/BF00164332>
- Sorbjan, Z., & Czerwinska, A. (2013). Statistics of turbulence in the stable boundary layer affected by gravity waves. *Boundary-Layer Meteorology*, *148*(1), 73–91. <https://doi.org/10.1007/s10546-013-9809-y>
- Sun, J., Burns, S. P., & Lenschow, D. H. (2002). Intermittent turbulence associated with a density current passage in the stable boundary layer. *Boundary-Layer Meteorology*, *105*(2), 199–219. <https://doi.org/10.1023/A:1019969131774>
- Sun, J., Lenschow, D. H., LeMone, M. A., & Mahrt, L. (2016). The role of large-coherent-eddy transport in the atmospheric surface layer based on CASES-99 observations. *Boundary-Layer Meteorology*, *160*(1), 83–111. <https://doi.org/10.1007/s10546-016-0134-0>
- Sun, J., Mahrt, L., Banta, R. M., & Pichugina, Y. L. (2012). Turbulence regimes and turbulence intermittency in the stable boundary layer during CASES-99. *Journal of the Atmospheric Sciences*, *69*(1), 338–351. <https://doi.org/10.1175/JAS-D-11-082.1>
- Van De Wiel, B. J. H., Moene, A. F., Steeneveld, G. J., Hartogensis, O. K., & Holtslag, A. A. M. (2007). Predicting the collapse of turbulence in stably stratified boundary layers. *Flow, Turbulence and Combustion*, *79*(3), 251–274. <https://doi.org/10.1007/s10494-007-9094-2>

- Vickers, D., & Mahrt, L. (2006). A solution for flux contamination by mesoscale motions with very weak turbulence. *Boundary-Layer Meteorology*, 118(3), 431–447. <https://doi.org/10.1007/s10546-005-9003-y>
- Yagüe, C., Viana, S., Maqueda, G., & Redondo, J. M. (2006). Influence of stability on the flux-profile relationships for wind speed, ϕ_m , and temperature, ϕ_n , for the stable atmospheric boundary layer. *Nonlinear Processes in Geophysics*, 13, 185–203. <https://doi.org/10.5194/npg-13-185-2006>
- Zhang, Q., & Liu, H. (2014). Seasonal changes in physical processes controlling evaporation over inland water. *Journal of Geophysical Research: Atmospheres*, 119, 9779–9792. <https://doi.org/10.1002/2014JD021797>